frontiers

Characterization of dissipative regions of a N-doped superconducting radio-frequency cavity

Eric M. Lechner [1,2], **Basu Dev Oli** [1], **Junki Makita** [3], **Gianluigi Ciovati** [2,3], **Alex Gurevich** [3] **and Maria Iavarone** [1,*]

[1] *Department of Physics, Temple University, Philadelphia, Pennsylvania, USA*
[2] *Thomas Jefferson National Accelerator Facility, Newport News, Virginia, USA*
[3] *Center for Accelerator Science, Department of Physics, Old Dominion University, Norfolk, Virginia, USA*

Correspondence*:
Department of Physics, Temple University, 1925 N 12th St., Philadelphia, Pennsylvania 19122, USA
iavarone@temple.edu

ABSTRACT

We report radio-frequency measurements of quality factors and temperature mapping of a nitrogen doped Nb superconducting RF cavity. Cavity cutouts of hot and cold spots were studied with low temperature scanning tunneling microscopy and spectroscopy, X-ray photoelectron spectroscopy and secondary electron microscopy. Temperature mapping revealed a substantial reduction of the residual resistance upon cooling the cavity with a greater temperature gradient and hysteretic losses at the quench location, pointing to trapped vortices as the dominant source of residual surface resistance.

Analysis of the tunneling spectra in the framework of a proximity effect theory shows that hot spots have a reduced pair potential and a wider distribution of the contact resistance between the Nb and the top Nb oxide. Alone, these degraded superconducting properties account for a much weaker excess dissipation as compared with the vortex contribution. Based on the correlation between the quasiparticle density of states and temperature mapping, we suggest that degraded superconducting properties may facilitate vortex nucleation or settling of trapped flux during cooling the cavity through the critical temperature.

Keywords: superconductivity, Superconducting RF Cavities, tunneling, microscopy, resonator, niobium

1 INTRODUCTION

Advances in Nb superconducting radio-frequency (SRF) cavity technology have pushed the quality factors Q_0 well above 10^{10} and the RF breakdown fields close to the dc superheating field H_s at GHz frequencies and temperatures T < 2 K [1, 2, 3, 4, 5, 6, 7]. Various surface and material treatments have been developed to improve the SRF performance of Nb cavities, including electropolishing, heat treatments, nanostructuring and impurity doping [1, 2, 3, 4]. These advances have drawn much attention to the fundamental limits of surface resistance R_s and maximum breakdown fields in a low-dissipative Meissner state. R_s in the Meissner state depends crucially on the quasiparticle density of states $N(E)$ [8, 9, 10]. It has been

shown that R_s could be reduced significantly by tuning $N(E)$ by pair-breaking mechanisms like subgap quasiparticle states in the bulk [9, 11, 12], Meissner screening currents [9, 13, 14], paramagnetic impurities [15, 16, 12], surface nanostructuring [17], local reduction of the pairing constant or a proximity-coupled normal suboxide layer at the surface [12].

Doping SRF cavities with impurities has been a very efficient way of producing Nb resonators with very high quality factors and RF breakdown fields [18, 19, 20, 21, 22, 23, 24, 25, 26, 27]. For instance, heating Nb SRF cavities in a ~ 25 mTorr atmosphere of pure nitrogen at 800 $^\circ$ C for a few minutes (referred to as "nitrogen doping") resulted in a quality factor $Q_0 > 2.5 \times 10^{10}$ at 1.3 GHz and 2 K at moderate accelerating gradients $E_{acc} \sim 16$ MV/m [20]. The N doping process has matured into a deployable process that has been successfully implemented in the LCLS-II upgrade [28]. It has been found that N-doped Nb cavities accumulate fewer hydrides since N occupies interstitial sites making hydride precipitation less favorable [29, 30, 31]. Addressing complex mechanisms by which N doping can affect the superconducting properties requires a surface scanning probe capable of tracking subtle changes in $N(E)$ caused by the materials treatment. Recently, point contact spectroscopy and low temperature scanning tunneling microscopy and spectroscopy (STM/STS) have been used to investigate Nb cavity cutouts [32, 33]. In the zero-temperature limit the tunneling conductance probes directly the quasiparticle density of states of the material's surface N_s, which determines the surface resistance. These studies have revealed changes in $N(E)$ in the first few nm at the surface of Nb cavities after N-doping [32, 33]. It was shown that N doping shrinks the metallic suboxide layer and reduces lateral inhomogeneities of the superconducting gap Δ and the contact resistance R_B between the suboxide and the Nb matrix, making R_B closer to an optimum value which minimizes R_s [12, 33]. At the same time, N doping slightly reduces Δ at the surface [32, 33].

Typically, the local R_s along the inner cavity surface is inhomogeneous, which manifests itself in hot-spots observed via temperature mapping of the outer cavity surface [34]. Hotspots reduce the global quality factor and may reduce the RF breakdown field by igniting lateral propagation of a hot normal zone along the cavity surface. Revealing the mechanisms of RF losses in hot-spots experimentally is challenging since the nature of RF losses is multifaceted. Hot-spots can result from lateral inhomogeneities of the complex oxide layer, the distribution of impurities or normal-conducting precipitates, such as nano-hydrides in the first few nm at the surface and pinned vortices. For instance, N-doping and materials heat treatments may produce islands of thicker metallic suboxides sandwiched between the dielectric oxide and the bulk Nb, causing an increased surface resistance [12, 17]. Trapped vortices threading the cavity wall during the cavity cooldown through T_c have been well-documented as one of the major sources of the residual surface resistance [1]. Long trapped vortices in hot-spots are pinned by materials defects in the bulk and the losses can come from vibrating vortex segments extending deep inside the cavity wall beyond the layer of RF field penetration $2\lambda \approx 100$ nm [35, 36]. In this case RF vortex losses are not localized in the first few nm at the surface and pinning defects trapping such vortices would be invisible to the surface scanning tunneling probes.

Addressing the mechanisms of RF losses in hot-spots thus requires a combination of experimental tools probing separately the surface hot-spots and bulk vortex hot-spots. The surface hot-spots caused by a nonuniform oxide layer and its effect on $N(E)$ after N doping can be directly probed by STM/STS. Vortex hot-spots can be probed by temperature mapping because, unlike the fixed materials defects, trapped vortices can be moved by temperature gradients [35, 37]. As a result, the strength of vortex hot-spots and their spatial distribution can change after cool-down of the cavity with different rates [38]. We use the combination of temperature mapping and scanning tunneling spectroscopy to address these questions.

In this paper, in contrast to previous electron tunneling measurements on N-doped Nb [32, 33], we investigate hot-spots with enhanced R_s identified by the JLab thermometry system during SRF testing of a N-doped cavity. Temperature mapping was used to observe the effect of the cavity cool-down rate on the strength and spatial distribution of hotspots. After RF measurements, cold and hot-spot cutouts were studied with the surface sensitive techniques of X-ray photoelectron spectroscopy (XPS), angle-resolved XPS (ARXPS) and low temperature STM/STS. Here XPS provides information about the chemical composition of the surface oxide layer while STM/STS probes the quasiparticle density of states, the superconducting gap, subgap states, as well as their spatial inhomogeneity [33]. The samples' surface was characterized with a scanning electron microscope (SEM) for any evidence of defects such as etch pits [39] or scarring due to hydrides [40] or nitrides [41, 42, 43, 44, 45].

2 SRF CAVITY TEST RESULTS AND SAMPLES

The cavity measured in this work was fabricated from ingot Nb from Tokyo Denkai, Japan, with residual resistivity ratio (RRR) of ~ 300 and large grains with size of a few cm^2. The cavity shape is that of the center cell of TESLA/EXFEL cavities [46]. Before N-doping, the cavity underwent standard buffered chemical polishing (BCP) and high pressure rinsing (HPR) with ultra-pure water. The cavity was N-doped by heating to 800 °C and exposing the cavity to a 25 mTorr nitrogen atmosphere for 30 minutes. After, the nitrogen was pumped-out and the cavity remained at 800 °C for 30 minutes, at which point the furnace heaters were turned off and the cavity was cooled naturally back to room temperature. Ultimately, ~ 10 μm were removed from the cavity's inner surface by electropolishing, followed by HPR, assembly of the end-flanges with RF feedthroughs and antennas in an ISO 4 clean room and evacuation on a vertical test stand. A temperature mapping system was attached to the outer cavity surface prior to insertion into a vertical test cryostat at Jefferson Lab [47].

2.1 Low-field surface resistance

The cavity was cooled with liquid He (LHe) and the cool-down rate was ∼1.5 K/min when the temperature at the bottom of the cavity crossed the critical temperature, $T_c \sim 9.25$ K. This resulted in a temperature gradient across the cell of ∼0.25 K/cm. After the cavity was fully immersed in LHe, the cavity quality factor was measured as a function of the He bath temperature, T_0, between $1.6 - 4.3$ K, while pumping on the LHe bath, and as a function of the peak surface magnetic field, B_p, (B_p/E_{acc} = 4.12 mT MV^{-1} m), between $5 - 20$ mT, using a phase-locked loop rf system. The average surface resistance of the cavity, R_s, was calculated from the measured Q_0 as $R_s = G/Q_0$, where $G = 270$ Ω is the cavity geometry factor. Figure 1 shows a plot of $R_s(T_0)$ for some B_p-values. The $R_s(T_0, B_p)$ data were analyzed following the same methodology described in Ref. [21] which showed that the reduction of R_s with increasing RF field is primarily due to the reduction of the pre-exponential factor $A(B_p)$ in the generic form of thermally activated surface resistance at $T << T_c$, $R_s(T_s) = Ae^{-U/k_BT_s} + R_i$, where U is the quasi-particle activation energy, T_s is the temperature of the RF surface, k_B is Boltzmann's constant and R_i is the residual resistance.

2.2 High-power rf test results

Figure 2 shows a plot of $Q_0(B_p)$ measured at 1.6 K in two consecutive cavity tests. The first test was performed after the first cool-down described in Sec. 2.1. The second test was performed after warming up the cavity to 80 K followed by a cool-down at a faster rate of ∼5 K/min, resulting in a larger temperature gradient of ~ 0.6 K/cm at T_c, across the cell. $Q_0(T_0)$ was also measured between $1.6 - 2.1$ K and $1 - 15$ mT after the second cool-down, prior to the rf test at higher power. The higher Q_0 in Test 2 compared to that

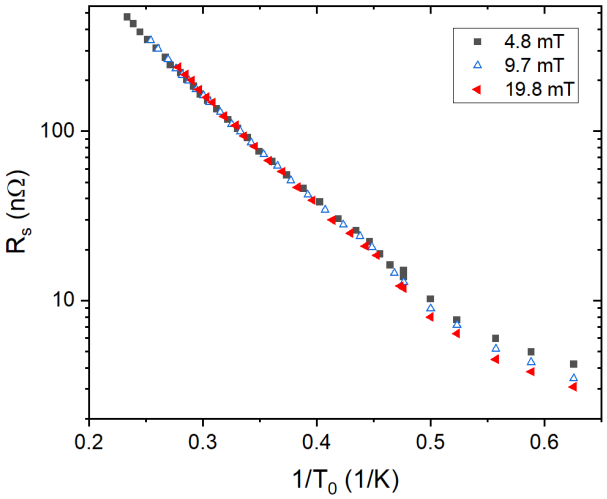

Figure 1. $R_s(T_0)$ measured for different B_p-values after the first cool-down.

of Test 1 is due to a lower residual resistance, decreasing from 3.4 nΩ to 2.4 nΩ. This reduction of R_i resulting from a faster cooling rate is related to better expulsion of the residual ambient magnetic field inside the cryostat [48], B_a, which was ∼0.2 μT during the experiments. Taking the difference of $1/Q(B_a)$ curves for these two tests we extract the additional surface resistance ΔR caused by the slower cooling rate. As shown in the inset in Figure 2, ΔR_s is practically independent of B_a, thus extra vortices trapped at a lower cooling rate do not produce additional nonlinearity in $R_s(B_a)$ in this field range.

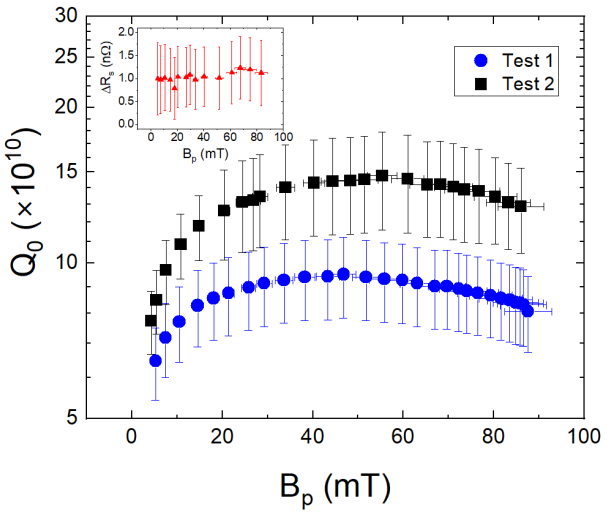

Figure 2. $Q_0(B_p)$ measured at 1.6 K after ∼1.5 K/min (Test 1) and ∼5 K/min (Test 2) cool-down rates across T_c. The inset shows the R_s-difference between Test 1 and Test 2 as a function of B_p.

The cavity performance was limited in both tests by a quench at $B_p \sim 86$ mT, without any field emission. The temperature maps measured just below the quench field are shown in Figure 3. The Q_0 at 1.6 K degraded by $\sim 17\%$ after quenching multiple times in Test 2. Such degradation corresponds to an increase of the residual resistance, R_i, by about 0.4 nΩ.

The quench location was the same in both tests, at temperature sensor No. 10 at the azimuthal angle of 220°. This location is ~ 2 cm away from the equatorial weld, in the high magnetic field region of the

cavity. Cold and hot-spot samples examined in this work were cut out from the same N-doped 1.3 GHz Nb superconducting cavity. The eight samples that were cut for this study are highlighted in white and labeled A-H on the temperature maps shown in Figure 3. Sample A was at the quench location.

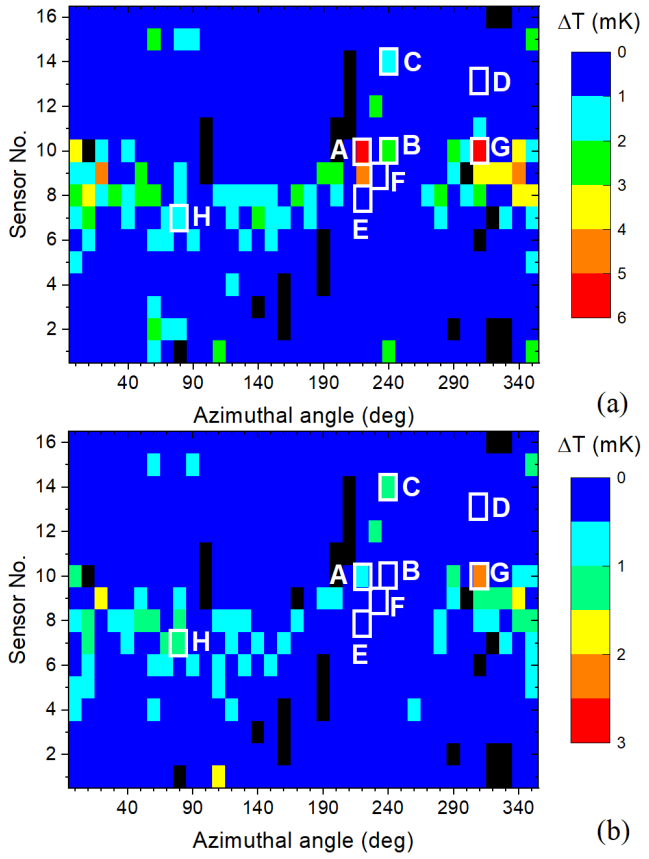

Figure 3. Unfolded temperature maps measured at 1.6 K and B_p ∼84 mT during Test 1 (a) and Test 2 (b) before quench. Sensor No. 8 is at the equator, No. 1 is at the bottom iris and No. 16 at the top beam tube, close to the iris. The location of the cut-out samples, labelled A-H are highlighted in white. Faulty sensor locations are shown in black.

Figure 4 shows the local temperature difference $\Delta T(B_p)$ between the cavity outer surface and the He bath at the location of the samples A-H, measured after Tests 1 and 2. The estimated combined systematic and statistical uncertainty in the temperature measurement is ∼1 mK. The magnitude of $\Delta T(B_p)$ at the hot-spot locations dropped significantly after Test 2. An increase in $\Delta T(B_p)$ was found at the location of sample A, for both tests, and of sample B for Test 2, after multiple quench events at the highest rf field. Hysteretic behavior of $\Delta T(B_p)$ at some locations of a different N-doped SRF cavity was also reported in Ref. [49]. The losses at the hot-spot locations can be characterized with a power law, $\Delta T \propto B_p^n$, where the exponent n obtained by the least square fit to the data was in the range of $2.1 - 2.4$ for Test 1 and $2.5 - 3.7$ for Test 2. Values of $n = 2.5 - 3.5$ were reported at hot-spot locations known to have trapped flux in an earlier study [50].

The samples used for XPS, STM and SEM characterization were cut from the cavity using a computer numerical control milling machine with no lubricant. During the cutting process, the samples were cooled by using a steady flow of compressed helium gas at the milling location. During the milling process the samples temperature did not raise above 32 °C. To ensure that the cutting process did not change the sample, a time-of-flight secondary ion mass spectrometry analysis was performed on a 16 × 16 mm^2 sample, and

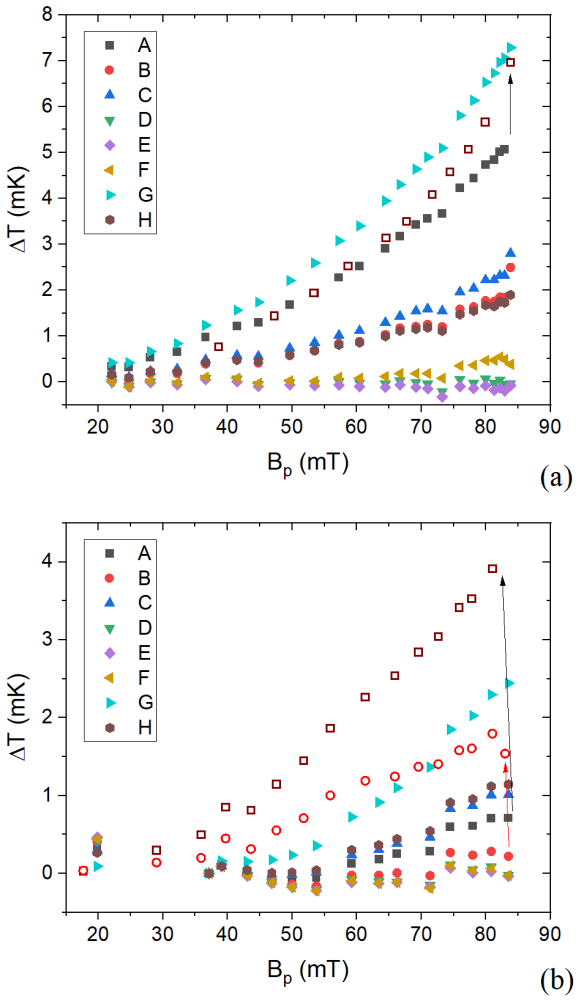

Figure 4. $\Delta T(B_p)$ measured at 1.6 K during Test 1 (a) and Test 2 (b) at the 8 locations chosen for cutouts. The empty symbols were measured at sample locations A and B while decreasing the rf field after quench, showing a hysteretic behavior. In the case of sample B, hysteretic behavior occurred only during Test 2.

Table 1. Surface characterization sequence for all of the samples cut from the N-doped Nb cavity, listed in the order in which they were performed.

Label	RF Dissipation	Analysis
A	Hot	XPS, SEM
B	Cold	XPS, SEM
C	Hot	STM
D	Cold	STM
E	Cold	STM, ARXPS
F	Cold	ARXPS
G	Hot	ARXPS, STM, SEM
H	Hot	ARXPS

the measurements were repeated near the same location after cutting out an 8×8 cm^2 sample. After the milling, an increase in carbon was found but new impurities were not. Table 1 shows the sequence of analysis done for each sample. The results from the XPS analysis of sample B and from the STM analysis of samples D and E have been previously reported in Ref. [33].

3 XPS AND SEM ANALYSIS

3.1 XPS analysis

A PHI Versaprobe 5000 XPS at the Drexel University Core Facilities was used for XPS measurements. The X-ray source used was Al K α (1486.6 eV, 200 W). The binding energy was calibrated to the adventitious carbon C 1s peak, corresponding to C-C bonds, at 284.6 eV. The depth profile was performed using Ar ion sputtering at 1 keV, 2 μA beam current and 2 mm × 2 mm beam size. We estimated a sputtering rate of 1.1 nm/min by atomic force microscopy (AFM).

The surface oxidation of Nb has been previously studied using XPS [51, 52, 53], ultraviolet photoemission [54], Auger electron spectroscopy [55, 56] and high-resolution electron energy loss spectroscopy [56]. These investigations have shown that NbO and NbO_2 are initially formed on Nb, with Nb_2O_5 being formed after further oxidation [51, 52, 53, 56, 57]. The oxidation state of Nb can be changed substantially after annealing in ultra-high vacuum or sputtering where Nb_2O_5 is reduced to NbO_2 and NbO due to the dissolution of O into the bulk [53, 26].

We studied the surface of hot-spot sample A and cold-spot sample B. A lower resolution survey was used to get information about the elements present on the surface. High resolution scans around peaks corresponding to the elements of interest were then performed with higher resolution to obtain the fine structure of the peaks, which contain the information about the chemical environment. In the survey spectrum of both samples there are visible peaks for O $1s$, Nb $3d$, Nb $3p$, Nb $3s$, Nb $4s$ and carbon C $1s$. The signal for the N $1s$ is not detectable in this low energy resolution spectrum.

High resolution XPS spectra for Nb $3d$ was carried out within 200–216 eV. The Nb $3d$ core level of the native surface of sample A (hot) and B (cold) showed slightly higher peaks for Nb_2O_5 for sample A. The Nb $3d$ peaks can be summarized as follows: Nb^{5+} (Nb_2O_5) peaks are located at 210.0 eV and 207.3 eV, Nb^{4+} (NbO_2) peaks are located at 208.8 eV and 206.0 eV, Nb^{2+} (NbO) peaks are located at 206.8 eV and 204.0 eV and Nb^0 peaks are at 205.0 eV and 202.2 eV [53]. Numerous oxygen vacancies exist in Nb_2O_5 [16, 51, 58]. Therefore, the Nb_2O_5 peaks are comprised of Nb_2O_5 and O-deficient Nb_2O_5 which makes it difficult to distinguish between the two from XPS spectra [59].

Although the oxidation states of metals can be altered by Ar ion bombardment [60], qualitative comparison between hot and cold spots subjected to the same procedure can provide useful insight into the material science of the surface. It has been shown that Ar ion sputtering of oxidized Nb removes oxygen preferentially from Nb_2O_5 and diffuses it into the bulk, which tends to thicken the lower oxidation state layers [61]. However, the ion current density used for the study in Ref. [61] is more than three orders of magnitude greater than the one we used, therefore we may expect less of a change in the oxide composition during Ar ion sputtering in our study.

Figure 5 shows the evolution of the Nb $3d$ spectral lines during Ar ion sputtering. The depth profile shown in Figure 5 reveals that sample A does not retain the higher oxides and reverts to the Nb^0 bulk relatively quickly compared to sample B that instead retains the higher oxide states.

In order to investigate the thickness of the native oxide and suboxides, ARXPS measurements were made with a PHI Quantera SXM-03 XPS at Virginia Tech's Nanoscale Characterization and Fabrication Laboratory. Samples E-H were rinsed with reagent grade ethanol and mounted in the XPS chamber by conductive carbon tape at the same time. Each was sputtered with 1 keV Ar for 30 s to remove surface carbon contamination, improving the signal-to-noise ratio for measuring the Nb $3d$ lines. The x-ray beam from the monochromator was focused to a 100 μm spot. For the variable angle data, at each position

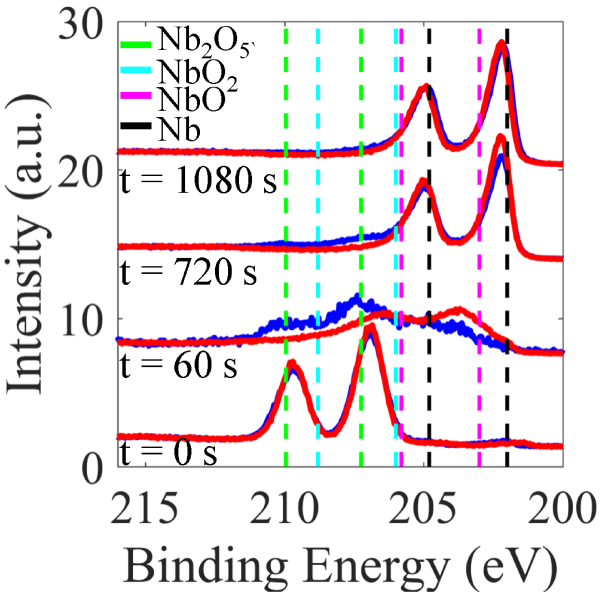

Figure 5. Evolution of the Nb $3d$ lines spectra acquired during depth profiling of hot-spot sample A (red) and cold-spot sample B (blue). From bottom to top, the XPS spectra were taken after sputtering times of 0 s, 60 s, 720 s and 1080 s, showing larger spectral weight for higher oxidation states in the cold spot while the hot-spot has a larger weight of low oxides, NbO_x around $\sim$ 203-204 eV especially near the surface. The Nb $3d3/2$ and Nb $3d5/2$ peaks of various oxidation states are shown with vertical dashed lines.

full survey scans were collected as 15 sweeps with pass energy set to 280 eV and step size at 1 eV. Measurements were taken at 15-90° angles at 15° increments. No significant difference was found among the 4 samples from the angle-resolved XPS spectra.

High resolution Nb $3d$ scans consisting of 20 sweeps with 13 eV pass energy and 0.025 eV step size were collected at 45° a take-off angle for each sample. The XPS curve fitting was performed in CasaXPS using a Shirley background and Gaussian-Lorentzian, GL(30), line shapes to determine chemical state and their contribution to the measured signal. The spin orbit splitting was taken as 2.72 eV and the ratio of intensities for the split lines was 2/3 [62]. Nb $3d$ spectra could be fit satisfactorily using three oxidation states, Nb_2O_5, NbO_2, NbO_x where x =0.4 - 0.6 [63], and Nb. Thicknesses of different oxide components were determined using the multilayer model [64]

$$d_i = \lambda_i \cos\theta \ln\left(1 + \frac{n_u \lambda_u}{n_i \lambda_i}\frac{F_i}{F_u}\right) T_2 T_3 ... T_{i-1}, \quad (1)$$

where subscript u represents the substrate, λ_i is the inelastic mean free path of layer i, θ is the electron take-off angle, n_i is the atomic density of the detected species and F_i is the spectral area of the signal related to layer i. T_i is the transmission coefficient which accounts for the attenuation through the preceding overlayer by $T_i = \exp\left(-d_i/\lambda_i \cos\theta\right)$. Values of the inelastic mean free path were estimated using the TPP-2M formula [65] and atomic densities were taken from [58]. The estimated thickness of the oxide components are listed in Table 2. More in-depth analysis have been performed in the NbO_x system [66, 67] which show that the Shirley background and Gaussian-Lorentzian line shapes have a thickness uncertainty of $\sim$ 10% for the thickness of each layer. Given this, no significant difference was found among the 4 samples.

Table 2. Thickness of the Nb oxides for samples E-H, determined from the deconvolution of the Nb $3d$ spectral lines measured by XPS at a 45° take-off angle.

Thickness [nm]	Sample E (Cold)	Sample F (Cold)	Sample G (Hot)	Sample H (Hot)
$d_{NbO_{0.4-0.6}}$	1.3	1.3	1.3	1.4
d_{NbO_2}	2.8	2.7	2.7	2.9
$d_{Nb_2O_5}$	1.7	1.5	1.5	1.4

3.2 SEM analysis

A FEI Quanta 450 FEG SEM was used for microscopy study of the rf surface of the cutout samples. The SEM images did not show any evidence for either niobium nitride or hydride features left on the surface. This is somewhat expected since it has been shown that nitrides are removed from the surface by $5-10$ μm EP and that most of the hydrogen is degassed from the Nb by the 800 °C vacuum annealing. Any residual hydrides have the size of a few nanometers, requiring high-resolution transmission electron microscopy to reveal them. The presence of a grain boundary was a distinctive feature observed on both samples A and G. The grain boundary found in sample A is shown in Figure 6.

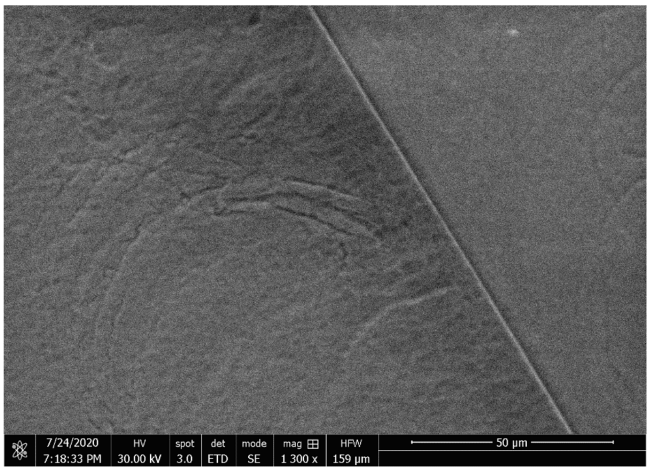

Figure 6. SEM image of sample A at 1300x magnification.

4 SCANNING TUNNELING SPECTROSCOPY

A Unisoku ultra-high vacuum STM system equipped with a 9 T superconducting magnet and with a base pressure of 4×10^{-11} Torr was used to perform low temperature scanning tunneling microscopy/spectroscopy (STM/STS) measurements between 1.0 K to 1.5 K. Pt-Ir tips prepared on Au were used in all measurements. The samples used for STM measurements are cold (Sample D) and hot (Sample C and G) spot cutouts from the same N-doped Nb cavity. Since the surface of Nb is dominated by a layer of a dielectric oxide Nb_2O_5, which is too thick to tunnel through, it is necessary to remove the dielectric layer by Ar ion sputtering. These samples were sputter-cleaned in a UHV sample preparation chamber attached to the STM chamber with a base pressure of low 10^{-11} Torr. Ar ion sputtering was performed using 99.999% pure Ar at a pressure of 10^{-5} Torr and accelerating voltage of 1 kV for 1 hour with a 4.75 μA beam current and 10 mm $\times$ 10 mm beam size. The removal rate was 0.27 nm/min as estimated by atomic force microscopy on a calibration sample. The Ar sputtering process removes the surface pentoxide and yields a metallic oxide surface NbOx a few nm thick. This surface can be studied by

STM that allows to study the local superconducting properties of the material. Clean and metallic surfaces are suitable for STM studies of local tunneling spectra as well as imaging of vortices, which leads to an estimate of the coherence length and mean free path. All differential conductance (dI/dV) measurements were made with the same tunneling parameters. The junction was stabilized at $V = 10$ mV, $I = 60$ pA and a standard lock-in technique was used with $V_{mod} = 200$ μV at 373.1 Hz.

Tunneling spectra were acquired on cold and hot spots N-doped Nb cutouts and analyzed in the framework of a proximity-coupled model which describes a thin metallic suboxide layer on the surface of a bulk superconductor [12]. We used the fitting procedure described in detail in [12, 33] to extract the density of states at the surface $N(E)$ from the tunneling spectra. The so-obtained $N(E)$ depends on the Dynes broadening parameter Γ [11] and two dimensionless parameters α and β, proportional to the thickness of the normal layer d and the contact resistance R_B between the normal layer and the superconductor:

$$\alpha = \frac{d}{\xi_s}\frac{N_n}{N_s}, \qquad \beta = \frac{4e^2}{\hbar} R_B N_n \Delta d \tag{2}$$

Here, $\xi_s = \sqrt{D_s/2\Delta}$ is the bulk coherence length, D_s is the electron diffusivity, N_s and N_n are the density of states at the Fermi surface in the normal state of the superconductor and normal layer respectively, $\Delta = \Delta_0 - \Gamma$ is the bulk pair potential and Δ_0 is the BCS gap at $T = 0$ K and $\Gamma = 0$.

Typical tunneling conductance spectra are shown in Figure 7(a) and (b) for sample C and D, respectively. The overall shape of these spectra, for cold and hot spots, differs significantly in the subgap region and in the shape and height of the coherence peak. Tunneling spectra were acquired on grids with a spacing of 32.6 nm over areas of 391 nm $\times$ 391 nm and 781 nm $\times$ 781 nm. Analysis of these spectra shows that the average Δ_0 is lower by $1\% - 2\%$ in the hot spot samples compared to the cold spot one. Furthermore, histograms of the extracted fit parameters clearly show that hot spots have wider distributions of α, β, Γ, Δ_0 than the cold spot. For instance, there is a low Δ_0 tail in the gap distribution in sample G, as shown in Figure 7(c), where the low Δ_0 values have been magnified to show the difference between cold and hot spots. The number of tunneling spectra acquired for sample D was 576, that for sample C was 720 and that of sample G was 1108. The Dynes broadening parameter Γ is found to be higher, on average, in the hot spot samples as supported by the wider distribution for samples C and G, presented in Figure 7(d). The α-distribution, shown in Figure 7(e) reveals that hot spots are more likely to have larger normal layers which tend to be detrimental and enhance the surface resistance [12, 18]. The parameter β (Figure 7(f)) in sample G exhibits a significant spread away from an optimum value of 0.3-0.4 at which a minimum in the surface resistance is predicted to occur [12].

STM grids on all samples investigated, also reveal the presence of near-surface defects that induce in-gap states in the quasiparticle density of states. Measurements of hot spot samples C and G reveal a significantly higher density of such defects. Example of these spectra are shown in Figure 8 where a line of spectra has been acquired along one of these extended defects on sample G. Zero-bias peaks and in-gap states in the quasiparticle density of states could indicate the presence of magnetic impurities [16] possibly associated with Nb suboxides [68].

To estimate the coherence length ξ_s and the mean free path l, a perpendicular magnetic field was applied to the sample's surface to generate Abrikosov vortices that modify the local density of states in the vortex core of $\simeq 2\xi_s$ in diameter. Vortices were imaged using STM by mapping the conductance at an energy where a vortex alters the density of states. Figure 9 (a) and (b) show the vortex lattice, imaged by acquiring the density of states at the Fermi energy, on cold spot sample D and hot spot sample C. Both samples

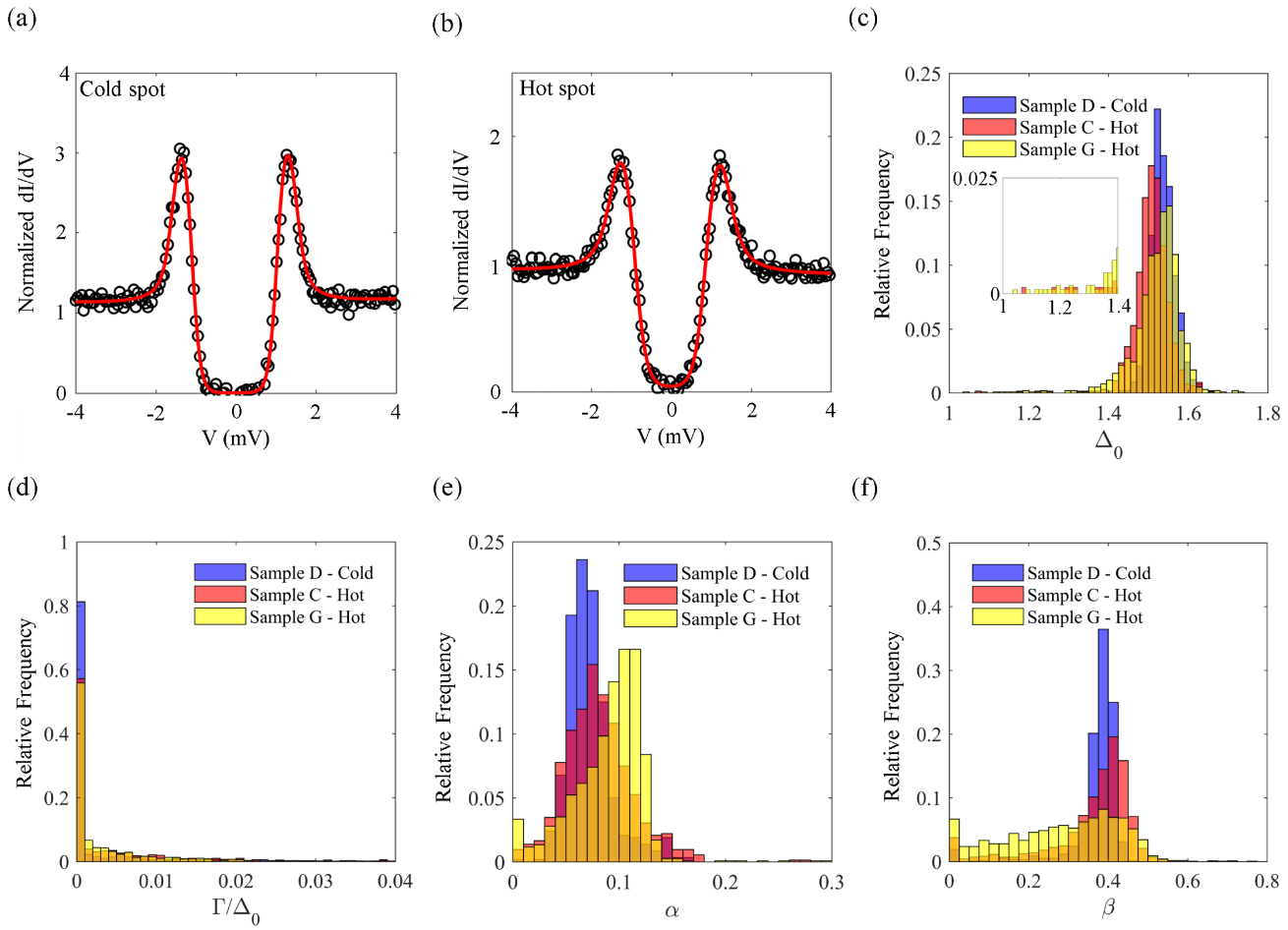

Figure 7. (a)-(b) Representative spectra for cold-spot sample D and hot-spot sample C from a N-doped Nb cavity. The red curves are the fit obtained using the proximity effect theory [12] and described in the text. The fitting parameters in (a) are: $\Delta_0 = 1.56$ meV, Γ =0 meV, $\alpha = 0.08$, $\beta = 0.39$, T =1.17 K. The fitting parameters in (b) are: $\Delta_0 = 1.51$ meV, Γ =0.03 meV, α =0.14, $\beta = 0.04$, $T = 1.45$ K . The results of the fitting procedure for all tunneling spectra acquired on cold and hot spot samples between 1.0 K and 1.5 K are summarized in the histogram comparison for the fit parameters Δ_0, Γ/Δ_0, α, and β reported in (c)-(f). In panel (c) the low Δ_0 values are shown magnified by a factor 10 to better visualize the difference between cold and hot spot results.

show a triangular vortex lattice consistent with theoretical predictions [69, 70]. Superconductors in the superclean limit, $l \gg \xi_0$, exhibit the Caroli-de Gennes-Matricon bound states localized in the vortex core [71, 72, 73], but those are not found here, indicating that the samples are in the dirty limit, $l < \xi_0$, where ξ_0 is the coherence length in the absence of impurities. Spatial analysis of the conductance around vortices $g(r)$ provides an estimate of ξ_s. The radial profiles shown in Figures 9(c) and (d) were obtained by averaging the azimuthally-averaged zero-bias conductance values around each vortex neglecting those on the borders. The value of ξ_s was obtained by fitting the averaged profile to $g = g_0 + Fe^{-r/\xi_s}$. Here, g_0 is the conductance far from the vortex core, F is a scaling factor, and r is the distance from the vortex core. This method provides a good measure of the bulk coherence length since the thin normal layer, $d \ll \xi_s$ does not significantly affect the vortex core diameter in the bulk [74, 75]. Using this procedure we obtain $\xi_s \cong (22 \pm 2)$ nm and (20 ± 2) nm for the N-doped Nb cold and hot spot, respectively, at H =0.15 T. This estimate is not far from others reported in literature [76, 77]. The slightly lower value of ξ_s that we obtained is consistent with a weak N-overdoping of our samples. The obtained values of the coherence

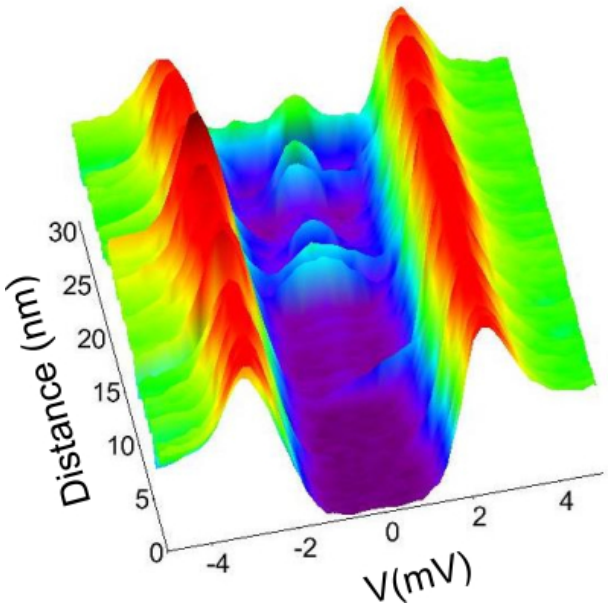

Figure 8. A line of 100 tunneling spectra acquired across an extended defect on hot-spot sample G. In all spectra the tip is stabilized at V_{set} =10 mV, I_{set} =60 pA, and the lock-in bias modulation V_{mod} =0.20 mV is used.

length indicate nearly the same mean free path in both samples. Using the relation $l < \xi_0^2/\xi_s$ and ξ_0 = 39 nm for clean Nb [78], we obtain $l \approx 11$ nm. We emphasize that the STM imaging of vortices probes l in the first few nm at the surface. By contrast, the BCS fits of the measured surface resistance give an averaged l in a much thicker layer $2\lambda \sim 100$ nm. Magneto-transport measurements of the upper critical field $H_{c2}(T)$ on Nb cutouts mostly probe the bulk l because a few μm thick N-doped Nb layer gives a negligible contribution to the global resistance of the 2-3 mm thick cavity wall. Generally, the vortex core radius is of the order of ξ_s but it is not exactly equal to the bulk coherence length [79], particularly at low temperatures $T \ll T_c$ and moderate disorder with only few impurities per Cooper pair $l \sim \xi_0$. In this case significant mesoscopic fluctuations of the vortex core shape can occur, consistent with the observed distribution of the vortex core shapes shown in Figures 9 and 10. Such mesoscopic fluctuations of the vortex core shape have been obtained in calculations of the DOS around vortex cores in the presence of randomly-distributed impurities with $l \sim \xi_0$ [80]. In this case extracting l from the averaged core size may give the mean free path different from that obtained from the BCS fit of $Rs(T)$, although both estimates do indicate that the N-doped cavities are in the dirty limit with $l \simeq (0.2 - 0.4)\xi_0$.

STM vortex images of Sample G show strong pinning and a distorted vortex lattice. Figure 10(a) shows a field-cooled vortex image taken at $H = 0.15$ T. Figure 10(b) shows instead an image of the same area after removal of the field without increasing the temperature. The image shows that vortices are trapped. Zero-field cooled images show absence of vortices in this area located approximately at the center of the sample. High resolution single vortex images have been used to determine the coherence length on sample G and yield a value of $\xi_s \cong (20 \pm 2)$ nm. The strong pinning found in this sample could explain the persistent excess RF dissipation found by T-mapping after both slow and fast cooldown.

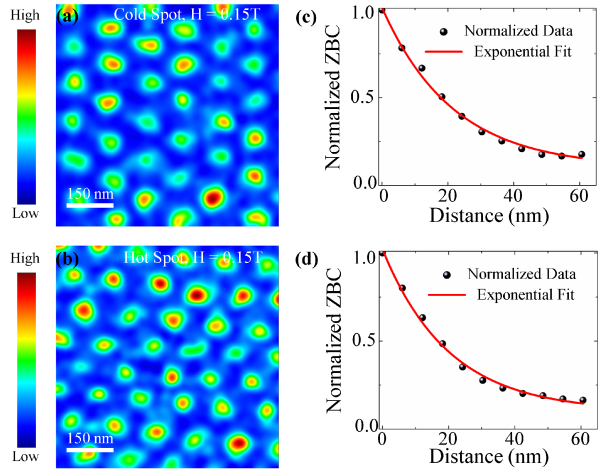

Figure 9. Normalized zero-bias conductance image showing vortices at $T = 1.5$ K and $H = 0.15$ T in N-doped Nb cold spot (a) and in the N-doped Nb hot spot (b). The scan area for both images is 697 nm $\times$ 697 nm and the magnetic field was applied normal to the surface. (c)-(d) Normalized zero bias conductance plotted as a function of distance from the vortex center for the cold and hot spot respectively. The solid lines are exponential fits to extract the coherence length. In all vortex images the tip is stabilized at V_{set} =10 mV, I_{set} =60 pA, and the lock-in bias modulation V_{mod} =0.20 mV is used.

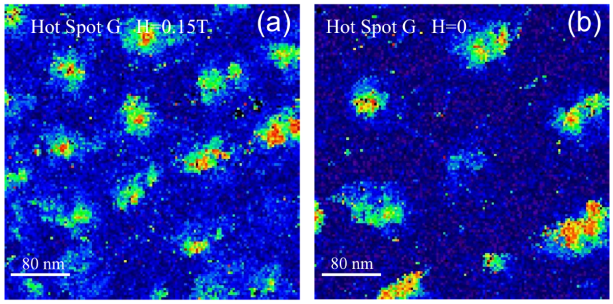

Figure 10. Normalized zero-bias conductance image showing vortices at $T = 1.5$ K and $H = 0.15$ T in N-doped Nb hot spot Sample G. (a) Field-cooled image at $H = 0.15$ T. (b) Conductance image of the same area after removal of the field without increasing the temperature ($H = 0$). The scan area for both images is 391 nm $\times$ 391 nm and the magnetic field was applied normal to the surface. The tip is stabilized at V_{set} =10 mV, I_{set} =60 pA, and the lock-in bias modulation $V_{mod} = 0.20$ mV is used.

5 ANALYSIS AND DISCUSSION

Our combined temperature mapping and scanning tunneling experiments have shown a complex interplay of both surface and bulk sources of RF losses in hot spots. The temperature mapping has shown that both the intensity of hot spots and their spatial distribution depends strongly on the cooldown rate of the cavity. This observation clearly demonstrates a significant contribution of trapped vortices to RF losses in hot spots. At the same time, our analysis of STM/STS and XPS experimental data has shown that hot spots regions exhibit weakly degraded superconducting properties at the surface with a wider distribution of superconducting gaps and a noticeable fraction of low-Δ regions.

A challenge common to all of the experimental studies found in the literature in which cavity cutout samples, identified by temperature mapping, have been analyzed by surface analytical methods is the difference between the spatial resolution of the thermometer and the size of area probed by surface analysis tools. The size of the thermometer used for temperature mapping is $\sim 8 \times 6$ mm^2, with the sensing portion

being a $\sim 4 \times 2$ mm^2 central area. This should be compared with the sub-μm^2 region probed by STM and the sub-mm^2 region probed by XPS. In this study, a statistically significant representation of the samples was achieved by performing STM measurements over nearly one thousand different spots near the center of each sample.

XPS measurements have revealed that the N-doped hot spot exhibits lower oxidation states of Nb deeper into the surface which may be the cause of a degraded interface resistance. The analysis of the STM spectra have shown that hot-spots may have a thicker normal suboxide and a non-optimum contact resistance between the suboxide and the bulk Nb. The hot-spot also suffers from a degraded Δ_0 with a fraction of particularly low Δ_0 regions which can significantly increase local RF losses. Moreover, the Dynes parameter Γ/Δ_0 turns out to be larger in the hot-spot, indicating stronger Cooper pairbreaking and larger surface resistance [12]. Yet our STM imaging of vortex cores shows that the electron mean free path is nearly the same in hot and cold-spots.

We used the model of a proximity-coupled normal layer on the surface of a bulk superconductor, which describes well the tunneling spectra, to calculate $R_s(T)$ with the parameters α, β, Γ and Δ_0 obtained from fitting the STM data [12]. Additional parameters in the model are the electrons' mean free path, the resistivity of the normal layer, ρ_n, and the Debye energy, $\Lambda = 23.6$ meV, the latter taken as a material constant. $l = 6.2$ nm was obtained from a least-squares fit of $R_s(T_0)$ at 4.8 mT with $R_s(T) = R_{BCS}(T) + R_i$, where $R_{BCS}(T)$ is the low-field Mattis-Bardeen surface resistance calculated numerically with Halbritter's code [81]. $\lambda_0 = 32$ nm, $\xi_0 = 39$ nm and $T_c = 9.25$ K were considered material constants for clean Nb and the mean value $\overline{\Delta_0} = 1.536$ meV from cold-spot sample D was used in the numerical calculation. The overheating of the RF surface at 4.8 mT is very weak, such that $T_s \approx T_0$.

The RF penetration depth and bulk coherence length used in the calculation of $R_s(T)$ with the proximity-coupled normal layer model were $\lambda = \lambda_0 \left(1 + 0.88\xi_0/l\right)^{1/2} = 81.8$ nm and $\xi_s = 0.74\xi_0 \left(1 + 0.88\xi_0/l\right)^{-1/2} = 11.3$ nm, respectively. ρ_n was used as a single fit parameter in the least-squares fit of the average cavity $R_s(T_0)$ measured at 4.8 mT with $R_s(T)$ from the model. The average values $\overline{\alpha} = 0.0723$, $\overline{\beta} = 0.37$, $\overline{\Gamma} = 0.0051$ meV and $\overline{\Delta_0} = 1.536$ meV obtained from STM data on cold-spot sample D were used in the numerical calculation of $R_s(T)$. The value of ρ_n from the fit was 0.5 $\mu\Omega$ cm and the calculated $R_s(T)$ is plotted in Figure 11(a), showing a good agreement with the experimental data down to ~ 1.8 K. The deviation at lower temperature is indicative of an additional contribution to the residual resistance, other than that from the normal layer, such as that due to trapped vortices. The thickness of the normal layer from Eq. (2), assuming $N_n \approx N_s$, is $d = \overline{\alpha}\xi_s = 0.8$ nm.

Following the same approach described above, we calculated R_s at 1.6 K for each set of parameters α, β, Γ and Δ_0 obtained from the STM data for cold-sample D and hot-spot samples C and G, resulting in the histograms shown in Figure 11(b). The median, mean and standard deviation from each sample are listed in Table 3. The median value of R_s(1.6 K) is ~ 2.8 nΩ for both hot-spot samples and ~ 2.1 nΩ for the cold-spot sample, compared to the global cavity $R_s = (3.8 \pm 0.3)$ nΩ measured in Test 2. The mean and standard deviation values are the highest for sample G, reflecting the wider spread in contact resistance values, the larger thickness of the normal layer and the higher tail towards lower values in the Δ_0-distribution from the STM data shown in Figure 7. There were a few parameter sets for sample G that resulted in R_s-values as high as $(0.1 - 2.9)$ $\mu\Omega$.

The contribution to the surface resistance at 1.6 K from the ideal BCS theory is (0.8 ± 0.2) nΩ, therefore the proximity-coupled normal layer contributes ~ 1.3 nΩ, corresponding to $\sim 43\%$ of the global, average residual resistance, based on the statistics from the cold spot sample. However, the local R_s-values obtained

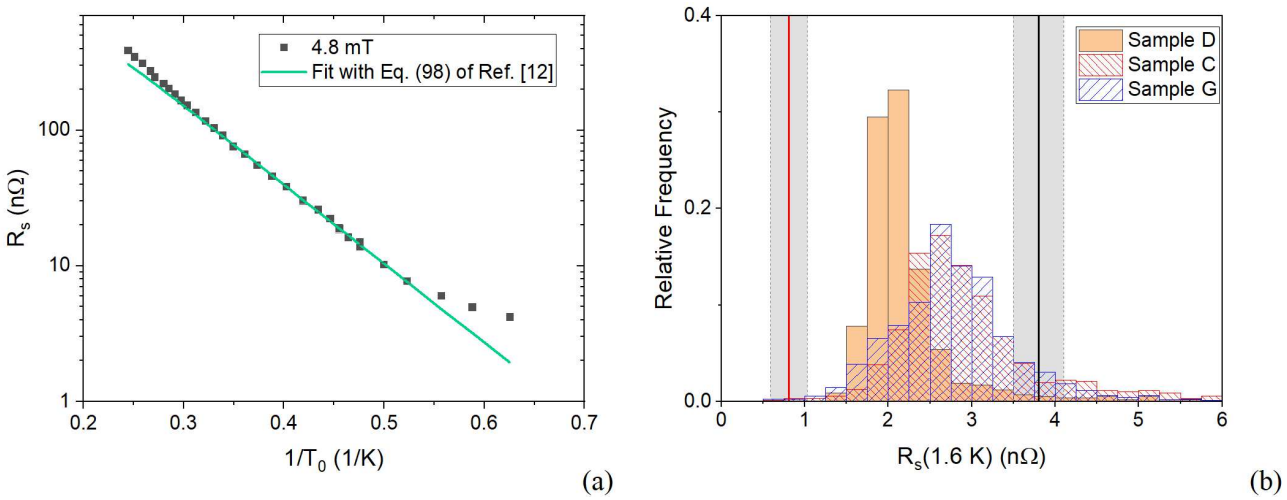

Figure 11. (a) Average cavity surface resistance as a function of LHe bath temperature, measured at 4.8 mT during Test 1 and $R_s(T)$ calculated with the model of Ref. [12] with the average parameters from cold spot D, $l = 6.2$ nm and $\rho_n = 0.5$ $\mu\Omega$ cm. The size of the error bars are about the same size of the symbols. (b) Histograms of R_s(1.6 K) calculated with the model of Ref. [12] for each set of parameters α, β, Γ, Δ_0 from the STM data for samples C, D and G. The solid black line is R_s(1.6 K) measured during Test 2, the solid red line is R_{BCS}(1.6 K) and the gray shaded areas represent $\pm 1\sigma$.

Table 3. Statistics on the surface resistance at 1.6 K calculated from the model of Ref. [12] for a proximity-coupled normal layer, using the model parameters obtained from STM data for samples C (hot-spot), D (cold-spot) and G (hot-spot).

Sample	Mean	Standard deviation	Median
D	2.6 nΩ	4.9 nΩ	2.1 nΩ
C	5.0 nΩ	15.9 nΩ	2.8 nΩ
G	12.7 nΩ	121 nΩ	2.8 nΩ

from the ΔT measured by temperature mapping can be significantly higher than the R_s-value averaged over the whole surface of the cavity, obtained from Q_0. The local R_s at the samples location can be obtained from the measured local ΔT from [82]:

$$R_{s,local} = \frac{2\Delta T_{local}}{H_0^2\,\eta} \tag{3}$$

where H_0 is the local surface RF magnetic field and η is the thermometers' efficiency. $\eta = 0.53$ K cm^2/W was obtained by a linear least-squares fit of ΔT, averaged over the outer surface, versus the RF power density. The local R_s at 80 mT at the locations of samples C and G was (8.8 ± 0.3) nΩ and (20.4 ± 0.6) nΩ for Test 2, respectively. Even higher local R_s-values were obtained at those locations during Test 1. These results clearly show that the additional RF dissipation in those hot spot locations is due to trapped vortices. This conclusion is consistent with the Arrhenius plot in Figure 11(a) which shows that the observed global residual resistance is higher than the prediction of the proximity model with the Dynes pairbreaking. This extra residual resistance is naturally produced by trapped vortices.

To evaluate the bulk and surface contributions to RF losses we use the following relation between the excess power P_0 in a hot-spot at the inner cavity surface and the resulting maximum value of ΔT observed by the temperature mapping on the outer cavity surface [35]:

$$\Delta T \approx \frac{P_0}{4\pi\kappa w} \ln \frac{4\kappa}{w h_K} \tag{4}$$

Here a hot-spot has a lateral size $L < L_h = \sqrt{w\kappa/h_K}$ and a thickness much smaller than the thickness w of the cavity wall, κ is the thermal conductivity, and h_K is the Kapitza thermal conductance between the cavity surface and the liquid coolant.

Using Eq. (4) we evaluate the number of vortices N which can produce the observed values of ΔT shown in Figure 3. Here the power P_0 generated by N sparse vortices under RF field at GHz frequencies f is given by [35]:

$$P_0 = \frac{N\pi B_p^2 \xi_s \lambda \sqrt{2\pi f \rho_s}}{\mu_0^{3/2} \left[\ln \frac{\lambda}{\xi_s} + \frac{1}{2}\right]^{1/2}} \tag{5}$$

where ρ_s is the normal state resistivity of Nb. Taking $w = 2.8$ mm, $\kappa \approx 7$ W/mK, $h_K \approx 2.5$ kW/m^{2}K at T = 1.6 K, we obtain the thermal length $L_h \simeq 2.8$ mm which defines the spatial scale of temperature spreading along the cavity surface from a local heat source. For f = 1.3 GHz, $B_p = 83$ mT, $\rho_s \simeq 7 \times 10^{-8}$ Ω m, and $\lambda/\xi_s \sim \lambda_0/l \simeq 4$ given by STM of vortices shown in Figure 9, we obtain from Eqs. (4) and (5) that $N \sim 8 \times 10^2 - 2 \times 10^3$ for $\Delta T \simeq 2 - 5$ mK in Test 1 and $N \sim 400$ for $\Delta T \simeq 1$ mK in Test 2. Assuming that trapped vortices are spaced by $\sim \lambda \simeq 80$ nm, we estimate sizes of vortex bundles as $L \sim \lambda\sqrt{N} \sim$ 1 - 10 μm. The data shown in Figure 3 thus indicate that cooling the cavity at a higher rate in Test 2 may reduce the numbers of trapped vortices in hot-spots by $\sim$ 2 - 5 times. Notice that Eq. (5) does not take into account pinning of vortices [83] which can increase the above estimate of N.

Another contribution to RF losses could come from the weakly deteriorated superconducting properties at the surface revealed by our STM measurements. Here the extra power $P_0 \simeq \pi L^2 \delta R H_p^2/2$ results from the change in the BCS surface resistance δR in the area of radius $\sim L$ due to the local reduction Δ and increase of the thickness of the normal suboxide layer illustrated by Figure 7. Here:

$$\delta R = \Sigma_i P_i R_i e^{-\Delta_i/k_B T} - R_0 e^{-\Delta_0/k_B T} \tag{6}$$

where P_i is a fraction of the hot spot area where α, β, Δ take particular values according to the histograms shown in Figure 7, and the last term in Eq. (6) describes the BCS surface resistance R_{BCS} for an ideal surface in the cold-spot areas. The pre-factor $R_i(\alpha_i, \beta_i, \Delta_i)$ in Eq. 6 is a rather complicated function of the parameters [12, 17], so we only make here a rough estimate of the size L of a surface hot-spot which could provide the observed ΔT values shown in Figure 3.

The reduction of the mean gap value from $\Delta_0 \approx 1.55$ meV in cold spots to $\langle\Delta\rangle \approx 1.5$ meV in hot-spots shown in Figure 7 increases R_s by the factor $e^{(\Delta_0 - \langle\Delta\rangle)/k_B T} \simeq 2.1$ at 1.6 K. In the model of [12] distributions of the metallic suboxide thickness and the contact resistance in the range of the parameters α and β shown in Figures 7(e) and (f) increases the mean prefactor $\langle R_i \rangle \approx$ by yet another factor $\sim$ 2-3, giving $\delta R \sim 5 R_{BCS} \sim 20$ nΩ at 1.6 K. From Eq. (4), it follows that

$$L \simeq \left[\frac{8\kappa w \mu_0^2 \Delta T}{\delta R B_p^2 \ln \frac{4\kappa}{w h_K}}\right]^{1/2} \tag{7}$$

For $\Delta T = 1$ mK, $B_p = 83$ mT and the above values of other parameters, Eq. 7 yields $L \simeq 1$ mm, more than 2 orders of magnitude larger than the size of the vortex hot-spots causing $\Delta T = 1$ mK. Thus, the changes in the surface superconducting properties revealed by STM give much weaker contributions to the observed temperature maps than trapped vortices. Yet our STM/STS measurements revealed a clear correlation between the weakly deteriorated superconducting properties at the surface and the positions of the hot-spots identified by temperature mapping. Moreover, the severity of the deterioration correlates with the inability to expel flux from that region during cooldown, as shown by the results from STM and T-maps on sample G. We suggest that, although the observed changes in the properties of the oxide layer and superconducting gap are not the prime sources of the RF power in the hot-spot sample, these parts of the cavity may be the regions where vortices first nucleate and then get trapped by bulk pinning centers upon cooling of the cavity through T_c. Another mechanism by which a reduced gap in hot-spots can be linked with trapped vortices may result from subsurface metallic nanohydrides [31, 77]. Due to the proximity effect [78], such metallic nanoparticles locally reduce $\Delta(T)$ over distances $\sim \xi_s$ around them. As a result, the nanoparticles that are closer than a few ξ_s to the surface not only can pin vortices but also cause a shadow effect of reduced Δ at the surface observed by STM.

The exponent $n > 2$ in the overheating $\Delta T \propto H^n$ can result from a temperature dependence of the surface resistance $R_s(T)$, even if R_s containing both the BCS and vortex contributions is independent of H. This follows from the uniform thermal balance equation $Y\Delta T = R_s(T)H^2/2$ which shows that $\Delta T(H)$ increases faster than H^2 if $R_s(T)$ increases with T. Here Y is the thermal conductance of the cavity wall [3].

The local overheating at the quench spot measured after the two cool-downs is fairly weak. Weak overhearing in a small flux hot-spot is proportional to the power in the hot-spot but the thermal breakdown field remains close to the uniform breakdown field without the hot-spot [3, 35]. The origin of the reduced quench field in N-doped cavities is not entirely clear and changes with the duration of N-exposure and of the post-annealing, impact the quench field [28, 84]. In addition to geometric magnetic field enhancement at grain boundaries and topographic defects, the reduction of the breakdown field of N-doped cavities can result from a dirtier surface, which reduces both H_{c1} and the superheating field H_s because the Ginzbug-Landau (GL) parameter $\kappa = \lambda/\xi$ increases as the mean free path decreases. For instance, $H_{c1} = [\ln(\kappa + C(\kappa)]\, H_c/\kappa\sqrt{2}$ decreases nearly inversely with κ, where the thermodynamic critical field H_c is independent of l and C decreases from 1.35 at $\kappa = 1/\sqrt{2}$ to 0.5 at $\kappa \gg 1$ [85]. In turn, the GL superheating field decreases from $H_s = 1.2H_c$ at $\kappa = 1$ in a clean Nb to $H_s = 0.745H_c$ at $\kappa \gg 1$ [86]. The reduction of H_s can locally reduce the surface barrier in a dirty island with higher concentration of impurities. Evidence for a reduced surface barrier in N-doped Nb samples was reported in Ref. [87].

6 CONCLUSIONS

Regions with different RF loss characteristics were located with thermometry mapping during the RF test of a N-doped Nb cavity. The cavity performance was limited by a quench at 86 mT and the quench location was the same after both slow and fast cooldown. A grain boundary was found at the quench location.

Cutouts from hot-spot regions were characterized by XPS and STM/STS measurements. The STM results can be described by a model which includes a thin proximity-coupled normal layer on top of the superconductor, resulting in a small degradation of both superconducting gap and degraded interface resistance in hot-spot regions, compared to cold-spot ones. The model parameters obtained from the STM measurements were used to calculate a distribution of R_s-values at 1.6 K. The thickness of the normal

layer was estimated to be of the order of 1 nm, contributing by ~ 1.3 nΩ to the average residual resistance extracted from RF measurements.

Our analysis of the experimental data suggests that weakly degraded superconducting properties at the surface of hot-spot regions are not the main source of RF losses, rather they are regions where vortices settle during cooldown. Vortex nucleation may also be preferential in theses locations but nucleation could also be facilitated by grain boundaries [88], such as found on samples A and G. While stronger thermal gradients will enhance flux expulsion as shown in Figure 3, poorly superconducting regions remain vulnerable to preferentially trapping vortices.

CONFLICT OF INTEREST STATEMENT

The authors declare that the research was conducted in the absence of any commercial or financial relationships that could be construed as a potential conflict of interest.

AUTHOR CONTRIBUTIONS

MI, GC, and AG contributed to conception and design of the study. MI, EL and BO did the STM, XPS and SEM measurements and data analysis. JM did the RF and thermometry measurements and data analysis. GC and AG contributed to the data analysis. MI and EL wrote the first draft of the manuscript. GC and AG wrote sections of the manuscript. All authors contributed to the final version of the manuscript.

FUNDING

This work was supported by the National Science Foundation, under award PHY-1734075. Some of the calculations were carried out on Temple University's HPC resources supported in part by the National Science Foundation through major research instrumentation grant N. 1625061 and by the US Army Research Laboratory under contract number W911NF-16-2-0189. G.C. is supported by Jefferson Science Associates, LLC under U.S. DOE Contract No. DE-AC05-06OR23177. The work of JM and AG at Old Dominion University was supported by DOE under grant DE-SC 100387-020.

ACKNOWLEDGEMENTS

The authors would like to acknowledge the use of the Core Facility at Drexel University for the XPS measurements, the Nano Instrumentation Center and Dmitriy A. Dikin at Temple University for the SEM measurements. The authors would also like to acknowledge M. Kelley and W. Leng for the ARXPS measurements at Virginia Tech.

DATA AVAILABILITY STATEMENT

The data that support the findings of this study are available from the corresponding author upon reasonable request.

REFERENCES

[1] Padamsee H, Knobloch J, Hays T. *RF Superconductivity for Accelerators* (VCH Verlag GmbH Co. KGaA, Weinheim) (2008).

[2] Antoine C. Materials and surface aspects in the development of SRF niobium cavities. Tech. Rep. EuCARD-BOO-2012-001, CEA Saclay (2012).

[3] Gurevich A. Superconducting radio-frequency fundamentals for particle accelerators. *Reviews of Accelerator Science and Technology* **05** (2012) 119–146. doi:10.1142/S1793626812300058.

[4] Padamsee HS. Superconducting radio-frequency cavities. *Annual review of nuclear and particle science* **64** (2014) 175–196.

[5] Singer W, Aderhold S, Ermakov A, Iversen J, Kostin D, Kreps G, et al. Development of large grain cavities. *Physical Review Special Topics-Accelerators and Beams* **16** (2013) 012003.

[6] Reschke D, Gubarev V, Schaffran J, Steder L, Walker N, Wenskat M, et al. Performance in the vertical test of the 832 nine-cell 1.3 GHz cavities for the european X-ray Free Electron Laser. *Phys. Rev. Accel. Beams* **20** (2017) 042004. doi:10.1103/PhysRevAccelBeams.20.042004.

[7] Dhakal P, Chetri S, Balachandran S, Lee PJ, Ciovati G. Effect of low temperature baking in nitrogen on the performance of a niobium superconducting radio frequency cavity. *Phys. Rev. Accel. Beams* **21** (2018) 032001. doi:10.1103/PhysRevAccelBeams.21.032001.

[8] Zmuidzinas J. Superconducting microresonators: Physics and applications. *Annu. Rev. Condens. Matter Phys.* **3** (2012) 169–214.

[9] Gurevich A. Tuning microwave losses in superconducting resonators. *Superconductor Science and Technology* **36** (2023) 063002. doi:10.1088/1361-6668/acc214.

[10] Mattis DC, Bardeen J. Theory of the anomalous skin effect in normal and superconducting metals. *Phys. Rev.* **111** (1958) 412–417. doi:10.1103/PhysRev.111.412.

[11] Dynes RC, Narayanamurti V, Garno JP. Direct measurement of quasiparticle-lifetime broadening in a strong-coupled superconductor. *Phys. Rev. Lett.* **41** (1978) 1509–1512. doi:10.1103/PhysRevLett.41.1509.

[12] Gurevich A, Kubo T. Surface impedance and optimum surface resistance of a superconductor with an imperfect surface. *Phys. Rev. B* **96** (2017) 184515. doi:10.1103/PhysRevB.96.184515.

[13] Gurevich A. Reduction of dissipative nonlinear conductivity of superconductors by static and microwave magnetic fields. *Phys. Rev. Lett.* **113** (2014) 087001. doi:10.1103/PhysRevLett.113.087001.

[14] Garfunkel MP. Surface impedance of Type-I superconductors: Calculation of the effect of a static magnetic field. *Phys. Rev.* **173** (1968) 516–525. doi:10.1103/PhysRev.173.516.

[15] Casalbuoni S, Knabbe E, Kötzler J, Lilje L, von Sawilski L, Schmüser P, et al. Surface superconductivity in niobium for superconducting rf cavities. *Nuclear Instruments and Methods in Physics Research Section A: Accelerators, Spectrometers, Detectors and Associated Equipment* **538** (2005) 45–64. doi:https://doi.org/10.1016/j.nima.2004.09.003.

[16] Proslier T, Kharitonov M, Pellin M, Zasadzinski J, Ciovati. Evidence of surface paramagnetism in niobium and consequences for the superconducting cavity surface impedance. *IEEE Transactions on Applied Superconductivity* **21** (2011) 2619–2622. doi:10.1109/TASC.2011.2107491.

[17] Kubo T, Gurevich A. Field-dependent nonlinear surface resistance and its optimization by surface nanostructuring in superconductors. *Phys. Rev. B* **100** (2019) 064522. doi:10.1103/PhysRevB.100.064522.

[18] Grassellino A, Romanenko A, Sergatskov D, Melnychuk O, Trenikhina Y, Crawford A, et al. Nitrogen and argon doping of niobium for superconducting radio frequency cavities: a pathway to highly efficient accelerating structures. *Superconductor Science and Technology* **26** (2013) 102001. doi:10.1088/0953-2048/26/10/102001.

[19] Romanenko A, Grassellino A, Crawford AC, Sergatskov DA, Melnychuk O. Ultra-high quality factors in superconducting niobium cavities in ambient magnetic fields up to 190 mG. *Applied Physics Letters* **105** (2014) 234103. doi:10.1063/1.4903808.

[20] Gonnella D, Eichhorn R, Furuta F, Ge M, Hall D, Ho V, et al. Nitrogen-doped 9-cell cavity performance in a test cryomodule for LCLS-II. *Journal of Applied Physics* **117** (2015) 023908. doi:10.1063/1.4905681.

[21] Ciovati G, Dhakal P, Gurevich A. Decrease of the surface resistance in superconducting niobium resonator cavities by the microwave field. *Applied Physics Letters* **104** (2014) 092601. doi:10.1063/1.4867339.

[22] Dhakal P, Ciovati G, Myneni GR, Gray KE, Groll N, Maheshwari P, et al. Effect of high temperature heat treatments on the quality factor of a large-grain superconducting radio-frequency niobium cavity. *Phys. Rev. ST Accel. Beams* **16** (2013) 042001. doi:10.1103/PhysRevSTAB.16.042001.

[23] Ciovati G, Dhakal P, Myneni GR. Superconducting radio-frequency cavities made from medium and low-purity niobium ingots. *Superconductor Science and Technology* **29** (2016) 064002. doi:10.1088/0953-2048/29/6/064002.

[24] Maniscalco JT, Gonnella D, Liepe M. The importance of the electron mean free path for superconducting radio-frequency cavities. *Journal of Applied Physics* **121** (2017) 043910. doi:10.1063/1.4974909.

[25] Posen S, Romanenko A, Grassellino A, Melnychuk O, Sergatskov D. Ultralow surface resistance via vacuum heat treatment of superconducting radio-frequency cavities. *Phys. Rev. Appl.* **13** (2020) 014024. doi:10.1103/PhysRevApplied.13.014024.

[26] Lechner EM, Angle JW, Stevie FA, Kelley MJ, Reece CE, Palczewski AD. Rf surface resistance tuning of superconducting niobium via thermal diffusion of native oxide. *Applied Physics Letters* **119** (2021) 082601. doi:10.1063/5.0059464.

[27] Dhakal P. Nitrogen doping and infusion in SRF cavities: A review. *Physics Open* **5** (2020) 100034. doi:https://doi.org/10.1016/j.physo.2020.100034.

[28] Gonnella D, Aderhold S, Burrill A, Daly E, Davis K, Grassellino A, et al. Industrialization of the nitrogen-doping preparation for SRF cavities for LCLS-II. *Nuclear Instruments and Methods in Physics Research Section A: Accelerators, Spectrometers, Detectors and Associated Equipment* **883** (2018) 143–150. doi:https://doi.org/10.1016/j.nima.2017.11.047.

[29] Garg P, Balachandran S, Adlakha I, Lee PJ, Bieler TR, Solanki KN. Revealing the role of nitrogen on hydride nucleation and stability in pure niobium using first-principles calculations. *Superconductor Science and Technology* **31** (2018) 115007. doi:10.1088/1361-6668/aae147.

[30] Pfeiffer G, Wipf H. The trapping of hydrogen in niobium by nitrogen interstitials. *Journal of Physics F: Metal Physics* **6** (1976) 167. doi:10.1088/0305-4608/6/2/013.

[31] Veit RD, Farber RG, Sitaraman NS, Arias TA, Sibener SJ. Suppression of nano-hydride growth on Nb(100) due to nitrogen doping. *The Journal of Chemical Physics* **152** (2020) 214703. doi:10.1063/5.0007042.

[32] Groll N, Ciovati G, Grassellino A, Romanenko A, Zasadzinski J, Proslier T. Insight into bulk niobium superconducting rf cavities performances by tunneling spectroscopy. *arXiv preprint arXiv:1805.06359* (2018).

[33] Lechner EM, Oli BD, Makita J, Ciovati G, Gurevich A, Iavarone M. Electron tunneling and x-ray photoelectron spectroscopy studies of the superconducting properties of nitrogen-doped niobium resonator cavities. *Phys. Rev. Appl.* **13** (2020) 044044. doi:10.1103/PhysRevApplied.13.044044.

[34] Knobloch J, Muller H, Padamsee H. Design of a high speed, high resolution thermometry system for 1.5 GHz superconducting radio frequency cavities. *Review of Scientific Instruments* **65** (1994) 3521–3527. doi:10.1063/1.1144532.

[35] Gurevich A, Ciovati G. Effect of vortex hotspots on the radio-frequency surface resistance of superconductors. *Phys. Rev. B* **87** (2013) 054502. doi:10.1103/PhysRevB.87.054502.

[36] Dhakal P, Ciovati G, Gurevich A. Flux expulsion in niobium superconducting radio-frequency cavities of different purity and essential contributions to the flux sensitivity. *Phys. Rev. Accel. Beams* **23** (2020) 023102. doi:10.1103/PhysRevAccelBeams.23.023102.

[37] Ciovati G, Gurevich A. Evidence of high-field radio-frequency hot spots due to trapped vortices in niobium cavities. *Phys. Rev. ST Accel. Beams* **11** (2008) 122001. doi:10.1103/PhysRevSTAB.11.122001.

[38] Martinello M, Romanenko A, Checchin M, Grassellino A, Crawford A, Melnychuk A, et al. Cooling dynamics through transition temperature of niobium SRF cavities captured by temperature mapping. *arXiv preprint arXiv:1504.04441* (2015).

[39] Zhao X, Ciovati G, Bieler TR. Characterization of etch pits found on a large-grain bulk niobium superconducting radio-frequency resonant cavity. *Phys. Rev. ST Accel. Beams* **13** (2010) 124701. doi:10.1103/PhysRevSTAB.13.124701.

[40] Barkov F, Romanenko A, Trenikhina Y, Grassellino A. Precipitation of hydrides in high purity niobium after different treatments. *Journal of Applied Physics* **114** (2013) 164904. doi:10.1063/1.4826901.

[41] Spradlin J, Palczewski A, Reece C, Tian H. Analysis of Surface Nitrides Created During Doping Heat Treatments of Niobium. *Proc. SRF'19* (JACoW Publishing, Geneva, Switzerland) (2019), no. 19 in International Conference on RF Superconductivity, 106–111. doi:10.18429/JACoW-SRF2019-MOP030. Https://doi.org/10.18429/JACoW-SRF2019-MOP030.

[42] Dhakal P, Ciovati G, Pudasaini U, Chetri S, Balachandran S, Lee PJ. Surface characterization of nitrogen-doped high purity niobium coupons compared with superconducting rf cavity performance. *Phys. Rev. Accel. Beams* **22** (2019) 122002. doi:10.1103/PhysRevAccelBeams.22.122002.

[43] Dangwal Pandey A, Dalla Lana Semione G, Prudnikava A, Keller TF, Noei H, Vonk V, et al. Surface characterization of nitrogen-doped Nb (100) large-grain superconducting RF cavity material. *Journal of Materials Science* **53** (2018) 10411. doi:10.1007/s10853-018-2310-8.

[44] Trenikhina Y, Grassellino A, Melnychuk O, Romanenko A. Characterization of Nitrogen Doping Recipes for the Nb SRF Cavities. *Proc. SRF'15*. JACoW (Geneva, Switzerland: JACoW) (2015), no. 17 in International Conference on RF Superconductivity, 223–227. doi:10.18429/JACoW-SRF2015-MOPB055.

[45] Yang L, Liu B, Ye Z, Yang C, Wang Z, Chen B, et al. Investigation into surface composition of nitrogen-doped niobium for superconducting rf cavities. *Nanotechnology* **32** (2021) 245701. doi:10.1088/1361-6528/abeb99.

[46] Aune B, Bandelmann R, Bloess D, Bonin B, Bosotti A, Champion M, et al. Superconducting TESLA cavities. *Phys. Rev. ST Accel. Beams* **3** (2000) 092001. doi:10.1103/PhysRevSTAB.3.092001.

[47] Ciovati G. *Investigation of the superconducting properties of niobium radio-frequency cavities* (Old Dominion University) (2005).

[48] Romanenko A, Grassellino A, Melnychuk O, Sergatskov DA. Dependence of the residual surface resistance of superconducting radio frequency cavities on the cooling dynamics around T_c. *Journal of Applied Physics* **115** (2014) 184903. doi:10.1063/1.4875655.

[49] Makita J, Ciovati G, Dhakal P. Temperature Mapping of Nitrogen-doped Niobium Superconducting Radiofrequency Cavities. *Proc. 6th International Particle Accelerator Conference (IPAC'15), Richmond, VA, USA, May 3-8, 2015* (Geneva, Switzerland: JACoW) (2015), no. 6 in International Particle Accelerator Conference, 3575–3577. doi:https://doi.org/10.18429/JACoW-IPAC2015-WEPWI038. Https://doi.org/10.18429/JACoW-IPAC2015-WEPWI038.

[50] Ciovati G, Gurevich A. Measurement of RF Losses Due to Trapped Flux in a Large-Grain Niobium Cavity. *Proc. SRF'07* (JACoW Publishing, Geneva, Switzerland) (????).

[51] Grundner M, Halbritter J. On the natural Nb2O5 growth on Nb at room temperature. *Surface Science* **136** (1984) 144–154. doi:https://doi.org/10.1016/0039-6028(84)90661-7.

[52] Hu Z, Li Y, Ji M, Wu J. The interaction of oxygen with niobium studied by XPS and UPS. *Solid State Communications* **71** (1989) 849–852. doi:https://doi.org/10.1016/0038-1098(89)90210-X.

[53] King B, Patel H, Gulino D, Tatarchuk B. Kinetic measurements of oxygen dissolution into niobium substrates: In situ x-ray photoelectron spectroscopy studies. *Thin Solid Films* **192** (1990) 351–369. doi:https://doi.org/10.1016/0040-6090(90)90079-S.

[54] Ciovati G. Effect of low-temperature baking on the radio-frequency properties of niobium superconducting cavities for particle accelerators. *Journal of Applied Physics* **96** (2004) 1591–1600. doi:10.1063/1.1767295.

[55] Farrell H, Isaacs H, Strongin M. The interaction of oxygen and nitrogen with the niobium (100) surface: Ii. reaction kinetics. *Surface Science* **38** (1973) 31–52. doi:https://doi.org/10.1016/0039-6028(73)90272-0.

[56] Franchy R, Bartke T, Gassmann P. The interaction of oxygen with Nb(110) at 300, 80 and 20 K. *Surface Science* **366** (1996) 60–70. doi:https://doi.org/10.1016/0039-6028(96)00781-9.

[57] Lindau I, Spicer WE. Oxidation of Nb as studied by the uv-photoemission technique. *Journal of Applied Physics* **45** (1974) 3720–3725. doi:10.1063/1.1663849.

[58] Halbritter J. On the oxidation and on the superconductivity of niobium. *Applied Physics A* **43** (1987) 1–28.

[59] Ohsawa T, Okubo J, Suzuki T, Kumigashira H, Oshima M, Hitosugi T. An n-type transparent conducting oxide: $Nb_{12}O_{29}$. *The Journal of Physical Chemistry C* **115** (2011) 16625–16629. doi:10.1021/jp203021u.

[60] Hashimoto S, Tanaka A. Alteration of Ti 2p XPS spectrum for titanium oxide by low-energy Ar ion bombardment. *Surface and Interface Analysis* **34** (2002) 262–265. doi:https://doi.org/10.1002/sia.1296.

[61] Karulkar PC. Effects of sputtering on the surface composition of niobium oxides. *Journal of Vacuum Science and Technology* **18** (1981) 169–174. doi:10.1116/1.570717.

[62] Chastain J, King Jr RC. Handbook of x-ray photoelectron spectroscopy. *Perkin-Elmer Corporation* **40** (1992) 221.

[63] Prudnikava A, Tamashevich Y, Babenkov S, Makarova A, Smirnov D, Aristov V, et al. Systematic study of niobium thermal treatments for superconducting radio frequency cavities employing x-ray photoelectron spectroscopy. *Superconductor Science and Technology* **35** (2022) 065019.

[64] Darlinski A, Halbritter J. Angle-resolved XPS studies of oxides at NbN, NbC, and Nb surfaces. *Surface and Interface Analysis* **10** (1987) 223–237. doi:https://doi.org/10.1002/sia.740100502.

[65] Tanuma S, Powell CJ, Penn DR. Calculations of electron inelastic mean free paths. V. Data for 14 organic compounds over the 50–2000 eV range. *Surface and Interface Analysis* **21** (1994) 165–176. doi:https://doi.org/10.1002/sia.740210302.

[66] Lubenchenko A, Batrakov A, Shurkaeva I, Pavolotsky A, Krause S, Ivanov D, et al. XPS study of niobium and niobium-nitride nanofilms. *Journal of Surface Investigation: X-ray, Synchrotron and Neutron Techniques* **12** (2018) 692–700.

[67] Lubenchenko AV, Batrakov AA, Pavolotsky AB, Lubenchenko OI, Ivanov DA. XPS study of multilayer multicomponent films. *Applied Surface Science* **427** (2018) 711–721.

[68] Cava RJ, Batlogg B, Krajewski JJ, Poulsen HF, Gammel P, Peck WF, et al. Electrical and magnetic properties of $Nb_2O_{5-\delta}$ crystallographic shear structures. *Phys. Rev. B* **44** (1991) 6973–6981. doi:10.1103/PhysRevB.44.6973.

[69] Blatter G, Feigel'man MV, Geshkenbein VB, Larkin AI, Vinokur VM. Vortices in high-temperature superconductors. *Rev. Mod. Phys.* **66** (1994) 1125–1388. doi:10.1103/RevModPhys.66.1125.

[70] Brandt EH. The flux-line lattice in superconductors. *Reports on Progress in Physics* **58** (1995) 1465. doi:10.1088/0034-4885/58/11/003.

[71] Caroli C, De Gennes P, Matricon J. Bound Fermion states on a vortex line in a type II superconductor. *Physics Letters* **9** (1964) 307–309. doi:https://doi.org/10.1016/0031-9163(64)90375-0.

[72] Hess HF, Robinson RB, Dynes RC, Valles JM, Waszczak JV. Scanning-Tunneling-Microscope Observation of the Abrikosov Flux Lattice and the Density of States near and inside a Fluxoid. *Phys. Rev. Lett.* **62** (1989) 214–216. doi:10.1103/PhysRevLett.62.214.

[73] Renner C, Kent AD, Niedermann P, Fischer O, Lévy F. Scanning tunneling spectroscopy of a vortex core from the clean to the dirty limit. *Phys. Rev. Lett.* **67** (1991) 1650–1652. doi:10.1103/PhysRevLett.67.1650.

[74] Stolyarov VS, Cren T, Brun C, Golovchanskiy IA, Skryabina OV, Kasatonov DI, et al. Expansion of a superconducting vortex core into a diffusive metal. *Nature communications* **9** (2018) 1–8.

[75] Gurevich A. Tuning vortex fluctuations and the resistive transition in superconducting films with a thin overlayer. *Phys. Rev. B* **98** (2018) 024506. doi:10.1103/PhysRevB.98.024506.

[76] Maniscalco J, Gonnella D, Hall D, Liepe M, Posen S. Measurements of Nb3Sn and nitrogen-doped niobium using physical property measurement system (2015).

[77] Yang Z, Lu X, He Y, Tan W, Huang S, Guo H. Magnetic properties and hydrides precipitation observation of nitrogen doping niobium used for accelerator applications. *Results in Physics* **12** (2019) 2155–2163. doi:https://doi.org/10.1016/j.rinp.2019.02.073.

[78] Tinkham M. *Introduction to superconductivity* (Courier Corporation) (2004).

[79] Sonier J. Muon spin rotation studies of electronic excitations and magnetism in the vortex cores of superconductors. *Rep. Prog. Phys.* **70** (2007) 1717. doi:10.1088/0034-4885/70/11/R01.

[80] Tamai T, Kato M. Local density of states of quasi-particles around a vortex core in a square superconducting plate with a random impurity potential. *J. Phys. Conf. Series* **1590** (2020) 012001. doi:10.1088/1742-6596/1590/1/012001.

[81] Halbritter J. FORTRAN-Program for the computation of the surface impedance of superconductors. Tech. Rep. FZK 3/70-6, Forschungszentrum Karlsruhe (1970).

[82] Knobloch J. *Advanced Thermometry Studies of Superconducting Radio-Frequency Cavities*. Ph.D. thesis, Cornell University (1997).

[83] Pathirana W, Gurevich A. Effect of random pinning on nonlinear dynamics and dissipation of a vortex driven by a strong microwave current. *Phys. Rev. B* **103** (2021) 184518. doi:10.1103/PhysRevB.87.054502.

[84] Maniscalco J, Aderhold S, Arkan T, Checchin M, Fuerst J, Gonnella D, et al. Statistical Modeling of Peak Accelerating Gradients in LCLS-II and LCLS-II-HE. *Proc. 20th International Conference on RF*

Superconductivity (SRF'21) (JACoW Publishing, Geneva, Switzerland) (2022), no. 20 in International Conference on RF Superconductivity, 804–808. doi:10.18429/JACoW-SRF2021-THPCAV009.

[85] Brandt EH. Properties of the ideal ginzburg-landau vortex lattice. *Phys. Rev. B* **68** (2003) 054506. doi:10.1103/PhysRevB.68.054506.

[86] Lin FPJ, Gurevich A. Effect of impurities on the superheating field of type-ii superconductors. *Phys. Rev. B* **85** (2012) 054513. doi:10.1103/PhysRevB.85.054513.

[87] Vostrikov A, Checchin M, Grassellino A, Kim Y, Romanenko A. Modifications of Superconducting Properties of Niobium Caused by Nitrogen Doping Recipes for High Q Cavities. *Proc. 6th International Particle Accelerator Conference (IPAC'15), Richmond, VA, USA, May 3-8, 2015* (Geneva, Switzerland: JACoW) (2015), no. 6 in International Particle Accelerator Conference, 3312–3314. doi:https://doi.org/10.18429/JACoW-IPAC2015-WEPTY022.

[88] Balachandran S, Polyanskii A, Chetri S, Dhakal P, Su YF, Sung ZH, et al. Direct evidence of microstructure dependence of magnetic flux trapping in niobium. *Scientific reports* **11** (2021) 1–12.